2010 American Control Conference
Marriott Waterfront, Baltimore, MD, USA
June 30-July 02, 2010

Control Model for Robotic Samara: Dynamics about a Coordinated Helical Turn

Evan R. Ulrich, Imraan Faruque, Jared Grauer, Darryll J. Pines, J. Sean Humbert, and James E. Hubbard Jr.

ABSTRACT

This paper details the flight dynamics and control of a prototype mono-wing rotorcraft that mimics the passive transit of the species of samara (winged seed), *Acer diabolicum Blume*. The asymmetric and all-rotating platform requires the development of a novel sensing and control framework. The general rigid body dynamics are separated into rotor dynamics and particle navigation, which are derived for a coordinated helical turn flight path. The equations of motion are used to calculate the forces necessary for flight along a trajectory recorded with a visual motion capture system. The result is a framework for state estimation and control, applicable to scaled versions of the robotic samara.

I. INTRODUCTION

IN recent years a new paradigm of flight has emerged which encompasses micro-scale bio-inspired aircraft. These highly maneuverable platforms are capable of hovering flight and are ideally suited for operation in a confined environment. The reconnaissance mission envisioned requires a high level of autonomy due to the fast dynamics of the vehicle and the limit on communication in the likely areas of operation, e.g. caves and buildings. Development of the equations of motion about a trimmed flight condition will facilitate future model-based controller and observer design, enabling autonomous operation.

Aerial systems that satisfy the dimensional constraints outlined by the DARPA "Nano Air Vehicle" (NAV) initiative[1] include fixed-wing, rotary-wing and flapping-wing vehicles. The simplest and most mature of these platforms are fixed-wing vehicles which boast speed, simplicity and well-known dynamics; however the necessity for forward flight restricts functionality in cluttered environments that can be traversed by rotary and flapping-wing platforms.

A substantial challenge in modeling the dynamics of micro-scale flight is the general lack of knowledge of the complex low Reynolds number flow regime they inhabit. The inherently three-dimensional flow of rotary wing vehicles cannot be adequately modeled using two-dimensional airfoil data, as lift production at this scale exceeds prediction [2]. The complexity of the system can be reduced substantially by identifying a linear model which describes its reaction to forces imposed by a control input. A model description of this nature lends itself well to modern control and state estimation.

This manuscript characterizes the forward flight dynamics and control of a rotary-wing NAV based on one of natures most efficient fliers: the seed of the maple (Acer) tree or samara. The work begins with a description of the vehicle and experimental setup. Then recorded flight test are shown and the characteristics of the flight path analyzed. Next the rigid body dynamics are derived for a flight path consisting of a helical turn. The equations of motion are then linearized about a trimmed flight condition, from which the small perturbation equations of motion can be expressed in canonical state space form. Equation-error and output-error methods are used to compute parameter estimates from flight data. The result of this work is a framework for state estimation and control.

Evan R. Ulrich (evanu@umd.edu), Imraan Faruque, Jared Grauer, J. Sean Humbert, and James E. Hubbard Jr. are with the Department of Aerospace Engineering, and Darryll J. Pines is the Dean of Engineering, University of Maryland, College Park, MD 20742 USA

II. MATERIALS AND METHODS

A. Monocopter Description

The concept of a single-wing rotating aircraft is not a new one, and in fact the first vehicle of this type was flown in 1952 in the woods surrounding Lake Placid, New York by Charles W. McCutchen [3]. A more recent vehicle, called the MAVPro, was developed and flown by a team led by Lockheed Martin Advanced Technology Laboratories, and was only capable of vertical flight [4]. The various single winged rotating aircraft developed over the years have made no attempt to utilize the most basic mode of transit of natural samara, autorotation. Additionally, airfoil cross sections and planform designs have had no similarity to that found in natural samaras.

Conventional monocopter designs apply torque to the vehicle with a thrust device slightly off-set from the $\hat{c}_y$-axis, and in the case of MAVPro the propeller spins in the $\hat{c}_y$-$\hat{c}_z$ plane and influences the stability about the $\hat{c}_y$-axis. This configuration results in the propeller fighting the pitch input from the flap and reduces controllability of the vehicle. The 3.5-inch diameter propeller of the robotic samara is spinning in the $\hat{c}_x$-$\hat{c}_z$ plane and opposes applied torque about the $\hat{c}_x$-axis providing additional roll stability. The configuration of the robotic samara permits control of rotation rate, altitude, and translation via the appropriate actuation of the wing servo. The component layout, and sign convention of the vehicle used in this study is shown in Figure 1.

The vehicle detailed in this study is a type of mono-wing rotorcraft modeled after the species of samara *Acer diabolicum Blume*. The layout of the vehicle consists of two rigid bodies linked by a servo allowing one rotational degree

978-1-4244-7425-7/10/$26.00 ©2010 AACC

of freedom. The first rigid body and main lifting surface resembles a scaled version of a samara both in planform geometry and airfoil cross section, [5] [6] [7] [8]. The second rigid body houses the electronics and motor/propellor unit applying a torque to rotate the vehicle as required for flight, Figure 1. The body fixed axis $[\hat{c}_x, \hat{c}_y, \hat{c}_z]$ and Euler angles $[\phi_w, \theta_w, \psi_w]$ describe the orientation of the vehicle, which is shown in Figure 1, along with the dimensions of the vehicle.

Flight of a monocopter differs from full scale helicopters as there exists no stationary frame of reference from which control inputs can be applied, i.e. helicopter swashplate. Control of the vehicle with once per revolution inputs requires knowledge of the vehicle's orientation relative to the desired flight path, but sensor packages capable of recording on-board flight data at the rate necessary for this type of control are not commercially available in the weight class required for use on nano-class vehicles. Instead, control algorithms development is based on state information collected externally using a visual motion capture system. This approach has been successful in identifying the pitch and heave dynamics of similar vehicle which is described in Ref. [9]. An approach to directional control which does not require the once per revolution actuation or high frequency measurement of vehicle orientation is discussed in detail in this paper.

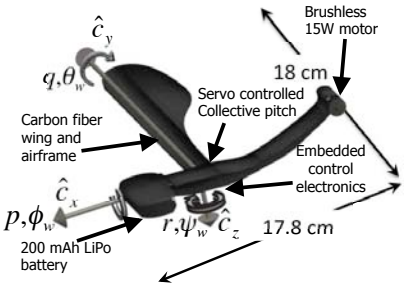

Fig. 1. Robotic samara orientation

Position and orientation of each vehicle was collected at a rate of 500 Hz using a visual tracking system. The open-loop control setup used to pilot the vehicle and record vehicle state information is discussed in Ref. [9]. During a flight test, the tracking system utilizes eight cameras to track the three-dimensional position of three retro-reflective markers placed on the samara wing. A model of the vehicle geometry and the exact locations of the markers are used for least-squares estimates of the position of the center of gravity as well as orientation. The open-loop control setup and measurement noise characteristics are detailed in Ref [9].

The obtained position estimates are exceptionally low noise. The position noise variance was estimated by recording data while not moving the vehicle. Inertial velocity estimates are calculated by differentiation of the inertial position, using a central difference scheme.

III. Flight Dynamics Model

A. Virtual body model

For the purposes of guidance, navigation, and control, a traditional MAV has a set of 6-7 configuration variables corresponding to the 3D position of the center of gravity and the remaining 3-4 used to describe the orientation of the vehicle relative to an inertial reference frame. For the robotic samara, the body orientation evolves over time, ranging from a steady rotation rate about the $\hat{\imath}_z$ axis in hover to a more complex pitching, rolling, flapping and rotating motion in other flight conditions such as the translational flight condition addressed in the study.

To simplify the description, consider instead the "disk" described by the motion of the wingtip over each revolution, or "tip path plane" (TPP). As defined in traditional rotorcraft analysis, the TPP considered is one that discards the harmonic motion higher than 1/rev, allowing a plane to be defined from the surface. The aerodynamic lift force may be considered to act perpendicular to the TPP.

To describe the dynamics of the samara, consider a virtual (rigid) body connected to the disc center with an ideal hinge, with its center of gravity (CG) located directly below the disc center and with the mass of the samara, as seen in Figure 2. No aerodynamic moments may be transmitted across an ideal hinge, splitting the position/orientation dynamics into *rotor dynamics* describing the flapping motion of the blade, and *positional dynamics* of the samara to be described using the translational equations of motion for the motion of a point mass acted upon by the rotor disc forces. The forward flight

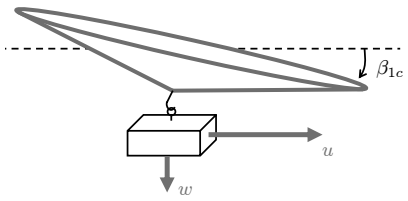

Fig. 2. Modeling the samara as a rotor with a hinged virtual body.

of the vehicle is most conveniently formulated in a non-rotating frame of reference attached to the virtual body. The orientation of the virtual body forward velocity u is defined by the projection of the velocity vector onto the $[\hat{\imath}_x, \hat{\imath}_y]$ plane so that translation can only occur in the u direction and $v = 0$. The heave velocity is parallel to the inertial $\hat{\imath}_z$ axis and is shown in Figure 3. Also shown is the equal and opposite definitions of aerodynamic incidence α, and the flight path angle γ in relation to the virtual body velocities, u, w. The cyclic blade flapping is defined as the angle between the wing and the inertial plane $[\hat{\imath}_x, \hat{\imath}_y]$ and is shown in Figure 5.

$$[u, v, w]^T = [V \cos\gamma, 0, -V \sin\gamma]^T \tag{1}$$

B. Equations of motion for a flapping blade

In steady hovering flight the coning angle $\beta = \beta_0 = constant$ and is independent of ψ. In forward flight the cyclically varying airloads induce an additional flapping

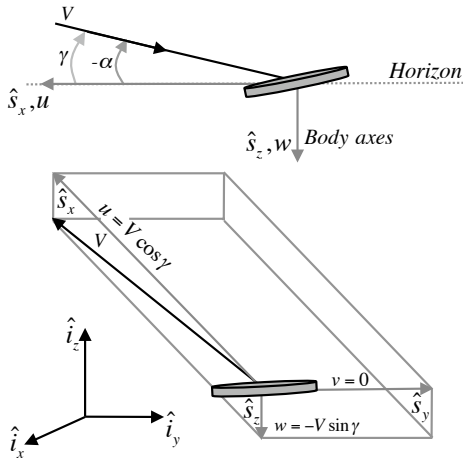

Fig. 3. Definition of angle of attack and sideslip angle in relation to the velocity components.

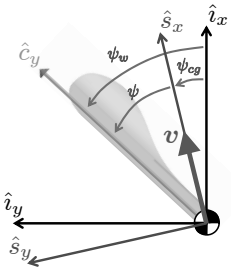

Fig. 4. Definition of azimuth angles of the wing ψ_w, virtual body ψ_{cg}, and virtual body with respect to the wing ψ.

response that varies about the azimuth ψ. The aerodynamic, centrifugal, and inertial forces acting on the robotic samara wing determine the observed coning angle, Figure 5. We define a positive moment as one which acts to reduce the β. The centrifugal force can then be written for an element along the span as $d(M_{CF}) = my^2\Omega^2\beta dy$ and the inertial moment about the flap hinge as $d(I) = my^2\ddot{\beta}dy$. Additionally the aerodynamic moment is $d(M_\beta) = -Lydy$. The sum of the applied moments form the differential equation describing the blade flapping motion. The flap equation can be written as a function of azimuth angle instead of time, where $\psi = \Omega t$ results in the following transformation; $\dot{\beta} = \Omega\overset{*}{\beta}$ and $\dot{\beta} = \Omega^2\overset{**}{\beta}$. The equation of motion of the robotic

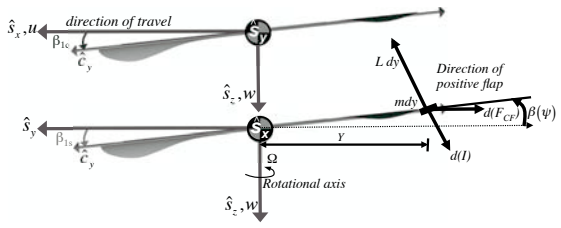

Fig. 5. Definition of coning angles β_{1s}, β_{1c}. with forces acting on an element of a flapping robotic samara wing

samara flapping wing reduces to

$$\overset{**}{\beta} + \frac{\gamma}{8}\overset{*}{\beta} + \beta = \frac{\gamma}{8}[\theta - \frac{4}{3}\lambda_i] \tag{2}$$

where γ is the lock number of the robotic samara. The lock number is a function of the aerodynamic and geometric parameters listed in Table I and is computed as

$$\gamma = \frac{\rho\, Cl_\alpha c R^4}{I_b} = 6.75. \tag{3}$$

Detailed numerical and steady state analytic solutions for the flap equation in (2) have demonstrated good agreement with a first order harmonic series [10]. Harmonic analysis of the flap equation allows a periodic solution of the form

$$\beta = \beta_0 + \beta_{1s}\sin(\psi) + \beta_{1c}\cos(\psi). \tag{4}$$

The blade flapping throughout the u-turn is observed to be periodic with respect to the azimuth angle ψ. The periodic coefficients describe the direction of force and can be seen to correlate with both the velocity and acceleration of the virtual body in Figure 6. The β_{1c} term influences the magnitude of u and the β_{1s} term influences the magnitude $\|\mathbf{V}_{cg}\|$. The coefficients β_{1s}, β_{1c} are the out of plane flapping angles that describe the orientation of the wing within the disk. The orientation of the virtual body defines the roll and pitch angles to be $\phi = \beta_{1s}$ and $\theta = \beta_{1c}$ respectively. Thus the flapping of the wing in forward flight describes the instantaneous orientation of the virtual body which includes the coning angle β_0.

TABLE I

ROBOTIC SAMARA WING PROPERTIES

Measurement	Symbol	Value	Unit
Air density	ρ	1.225	Kg/m^3
Mean chord	c	3.5	cm
Wing length	R	18	cm
Lift curve slope	$C_{l\alpha}$	3.5	-
Wing inertia	I_b	23.3μ	Kgm^3

C. Rigid body equations of motion

The rigid body equations of motion are differential equations that describe the evolution of the state variables subject to applied forces. In body-fixed axes the sum of all external forces applied to the center of gravity is

$$m\dot{\mathbf{V}}_{cg} + mS(\boldsymbol{\omega})\mathbf{V}_{cg} = \mathbf{f} \tag{5}$$

where m is the vehicle mass, $\mathbf{V}_{cg} = u\hat{s}_x + v\hat{s}_y + w\hat{s}_z$ is the translational velocity of the center of gravity, $\boldsymbol{\omega} = p\hat{s}_x + q\hat{s}_y + r\hat{s}_x$ are the body-fixed roll, pitch and yaw rates, $\mathbf{f} = f_x\hat{s}_x + f_y\hat{s}_y + f_z\hat{s}_z$ are externally applied forces, and $S(.)$ is a skew operator. The rotational dynamics are governed by the differential equation

$$\mathbf{I}\dot{\boldsymbol{\omega}} + S(\boldsymbol{\omega})\mathbf{I}\boldsymbol{\omega} = \boldsymbol{\tau} \tag{6}$$

where $\boldsymbol{\tau}$ is a vector of externally applied torques and $\mathbf{I}$ is a diagonal inertia matrix arising from symmetries in the virtual aircraft.

D. Coordinated helical turn

The flight path of the vehicle resembles a steady banked turn such that $\dot{\phi}_0$ and $\dot{\theta}_0$ are equal to zero. Additionally γ the flight path angle (> 0 for climbing flight) is small so that $\sin\gamma = \gamma$ and $\cos\gamma = 1$. The kinematic equations are then

$$p = -\dot{\psi}_{cg} \sin\beta_{1c} \tag{7}$$

$$q = \dot{\psi}_{cg} \cos\beta_{1c} \sin\beta_{1s} \tag{8}$$

$$r = \dot{\psi}_{cg} \cos\beta_{1c} \cos\beta_{1s}. \tag{9}$$

Substituting the derived velocities and modified kinematics into the force equilibrium equations results in the following equations of motion:

$$X = mg \sin\beta_{1c} + m(\dot{u} + wq - vr) \tag{10}$$

$$Y = -mg \cos\beta_{1c} \sin\beta_{1s} + m(\dot{v} + ur - wp) \tag{11}$$

$$Z = -mg \cos\beta_{1c} \cos\beta_{1s} + m(\dot{w} + vp - uq) \tag{12}$$

where $[X, Y, Z]^T$ represent force equilibrium in the body fixed coordinate frame, and g is acceleration due to gravity.

Flight tests conducted with the robotic samara provide a means of verifying the equations of motion. A portion of a flight which fits within the constraints of the proposed analytical model is shown in Figure 6.

The variation of $\dot{\psi}_{cg}$ with the turn radius r_{turn} is observed to be linear for most of the trial, where a small but linear change in r_{turn} corresponds to a large change in turn rate $\dot{\psi}_{cg}$. The final portion of the figure shows the linear change in forward speed derivative $\dot{u}$ with respect to r_{turn}.

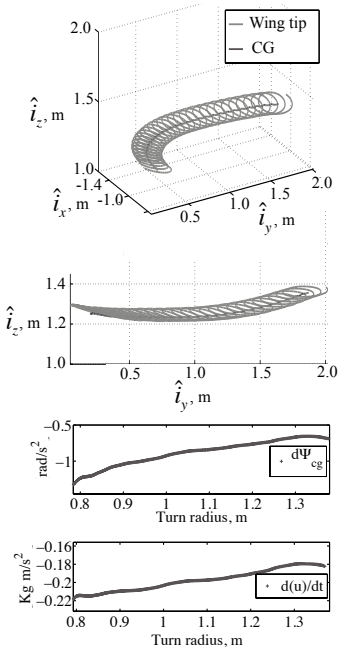

Fig. 6. Flight data for a steady helical turn, including turn radius r_{turn}, turn rate $\dot{\psi}_{cg}$.

E. Extension to forward flight

1) Pure longitudinal motion: Consider now straight flight as a special case of a coordinated turn, where $\dot{\psi} = p_0 = q_0 = r_0 = \beta_{1s} = 0$. The equation of motion along the $\hat{s}_x$-axis for forward flight may be written as the combination of a nominal condition (represented by $[]_0$) and a small perturbation $\Delta[]$ as:

$$X_0 + \Delta X - mg[\sin(\beta_{1c0}) + \Delta\beta_{1c}\cos(\beta_{1c0})] = \Delta\dot{u} \tag{13}$$

Setting all perturbation quantities to zero $\Delta[]$=0 yields the force equilibrium along trimmed forward flight:

$$\frac{X_0}{m} = g \sin\beta_{1c0} \tag{14}$$

2) Perturbation equations: The trimmed forward flight equation 14 can be subtracted from the linearized force equilibrium equation 13 leading to a description of small perturbation motion about the equilibrium condition as:

$$\Delta\dot{u} = \frac{\Delta X}{m} - g\Delta\beta_{1c}\cos\beta_{1c} \tag{15}$$

Separating out the linear effects of the longitudinal variables $[u, w, \beta_0, \beta_{1c}]$ facilitates development of a canonical linear control model, and can be written as:

$$\frac{\Delta X}{m} = X_u\Delta u + X_w\Delta w + X_{\beta_0}\Delta\beta_0 + X_{\beta_{1c}}\Delta\beta_{1c} + X_\theta\Delta\theta, \tag{16}$$

where $X_{[.]}$=$(1/m)\partial X/\partial[.]$. The time-invariant linear system can now be expressed in state space form $\dot{\mathbf{x}} = \mathbf{A}\mathbf{x} + \mathbf{B}\mathbf{u}$ where $\mathbf{x} = [\Delta u, \Delta w, \Delta\beta_0, \Delta\beta_{1c}]^T$, and $\mathbf{u} = [\Delta\theta_0]$, written in matrix form as:

$$[\ A\ ] = \begin{bmatrix} X_u & X_w & 0 & 0 & 0 \\ 0 & 0 & Z_\Omega & Z_{\beta_0} & 0 \\ 0 & 0 & \Omega_\Omega & \Omega_{\beta_0} & 0 \\ 0 & 0 & \beta_{0\Omega} & 0 & 0 \\ \beta_{1c_u} & 0 & \beta_{1c_\Omega} & \beta_{1c_{\beta_0}} & 0 \end{bmatrix} \tag{17}$$

and $[B] = [X_{\theta_0}, Z_{\theta_0}, 0, \beta_{0\theta_0}, 0]^T$.

TABLE II
PARAMETER ESTIMATES AND STANDARD ERRORS

Parameter θ	Equation-Error $\hat{\theta} \pm s(\hat{\theta})$	Output-Error $\hat{\theta} \pm s(\hat{\theta})$
X_u	$+0.4165 \pm 0.1753$	$+0.8978 \pm 0.3416$
X_w	$+3.7378 \pm 0.5694$	$+1.6108 \pm 0.4431$
X_{θ_0}	-7.9875 ± 21.055	$+114.35 \pm 25.827$
Z_Ω	$+0.2538 \pm 0.0164$	$+0.2237 \pm 0.0318$
Z_{β_0}	-57.323 ± 12.301	-17.695 ± 23.318
Z_{θ_0}	-14.718 ± 13.399	$+38.942 \pm 19.449$
Ω_Ω	-1.3358 ± 0.2084	-2.2649 ± 0.5876
Ω_{β_0}	$+1001.5 \pm 63.791$	$+1231.1 \pm 219.49$
$\beta_{0\Omega}$	-0.0081 ± 0.0008	-0.0063 ± 0.0008
$\beta_{0\theta_0}$	-1.8922 ± 0.3399	-2.3455 ± 0.3158
β_{1c_u}	-0.5881 ± 0.2122	$+0.5628 \pm 0.2050$
β_{1c_Ω}	-0.1145 ± 0.0325	$+0.0872 \pm 0.0540$
$\beta_{1c_{\beta_0}}$	$+24.323 \pm 7.7405$	-22.543 ± 15.787

IV. Experimental Results

Lateral directional flight was recorded in the laboratory for a flight path consisting of an initial trim state and a perturbation about the trim, Figure 7. In general, the turn radius is inversely proportional to the collective pitch of the wing. The samara travels in the opposite direction of the motion that would be induced by an impulsive collective input applied at that instant. A non-impulsive, sustained input changes the turn radius of the flight path such that an alternating series of large and small turn radii can steer the vehicle in a specific direction.

The velocity components, rotation rate, and blade flap angles are shown in Figure 7 as they vary with the input θ_0. The first 0.5s of flight correspond to a near constant u and near zero w. At the time of the u-turn, 1-1.5s, there is an increase in the vertical velocity. The increase is correlated because a collective pitch increase used to change the heave velocity, is also used to change the flight path direction. The

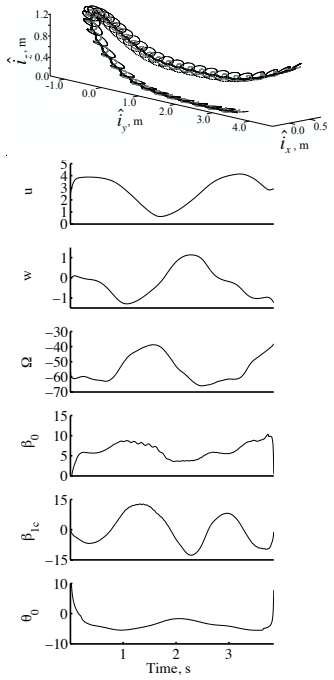

Fig. 7. State trajectories in a coordinated turn.

flight data shown in Figure 7 was used to perform system identification using algorithms implemented in a MATLAB toolbox called System IDentification Programs for AirCraft (SIDPAC), detailed in Reference[11]. Guided by analytical modeling, modified step-wise regression was used to determine the model structure using the statistical significance of measured states, resulting in the system shown in (**??**). This model structure was chosen to maximize the model fit using regressors with a significant partial-f ratio, while minimizing the parameter estimate error bounds. A two-step procedure using the equation-error method, followed by the output-error method, was used to estimate the stability derivatives in the model. The equation-error method performs a linear estimation at the acceleration level, which has a deterministic solution that is cheap to compute. The output-error method, widely regarded as more accurate, performs a nonlinear estimation at the level at which measurements were taken. This method requires an iterative numerical solver, but intial guesses using an equation-error estimate typically converge quickly. Parameter estimates and standard errors, corrected for non-white colored residuals, are given in Table II. Model fits to the perturbation data sets are shown in Figure 8 and 9 for the equation-error and output-error methods, where the measurements are plotted with a solid line and the model outputs are plotted with a dashed line.

An acceptable fit was achieved between the analyzed data and many of the model structure and parameter estimates. The equation-error results had model fits of 0.94, 0.94, 0.91, 0.56, and 0.59 for matching $\dot{\mathbf{x}}$ measurements and fits of 0.85, 0.97, 0.92, 0.83 and 0.12 for matching $\mathbf{x}$ measurements. The equations describing the flap dynamics had low model fits for both methods. Several parameters were estimated consistently by the two methods, lying within two standard deviations of each other.

Significant insight may be obtained from the estimates that did not match well or had large error bounds. Much of the inconsistency may be attributed to limited excitation present in the flight data, but it also reveals an important characteristic about the analyzed flight data. For example, the finding that the stability derivative X_u is positive indicates a rare case of forward speed instability. Forward speed instability is normally a localized result and not found in a general flight dynamics result. In this case, the portion of linearized flight used in the equation-error output method fit included a portion of descending flight, during which the robotic samara (a global stability) exhibits a local instability with respect to forward speed, because arresting a forward velocity requires the rotor disc first be inclined to oppose the motion. The estimated error in this term reflects the fact that the stability derivative was required to fit a more general flight case, but is biased toward descending flight. In general, the results do show promise for identifying samara flight dynamics in this manner and will be improved in the future with flight tests better suited for system identification.

V. Conclusion

This paper presents the derivation of the equations of motion of a robotic samara designed and tested at the University of Maryland, College Park. The nonlinear Euler equations were used to describe the rigid body dynamics of the vehicle in a steady turn. The rotating wing motion was treated as simple harmonic oscillator and coupled to the virtual body equations of motion which combine to form a set of seven nonlinear differential equations. The equations of motion for the steady turn are extended to forward flight and linearized about a trim state, resulting in five linearized small perturbation equations in state space form. Flight tests provided high accuracy position information that was reduced to wing flap angles and virtual body velocities. This information was used to specify a flight condition that fit within the limits of the derived model allowing for estimation of the

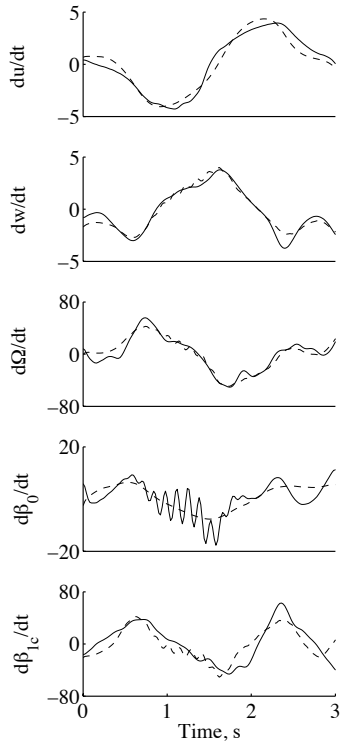

Fig. 8. Equation-error model fit to perturbation data.

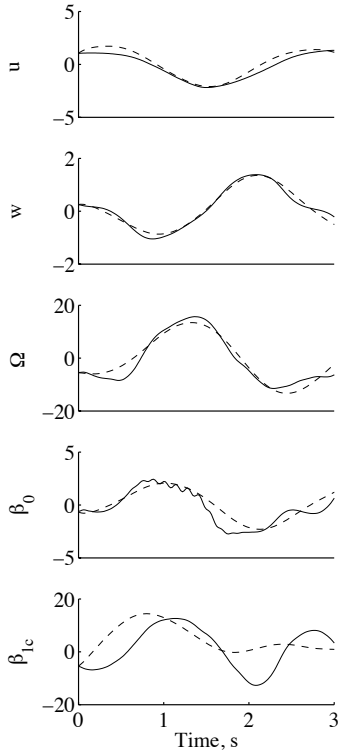

Fig. 9. Output-error fit to perturbation data.

parameters defined in the $\mathbf{A}$ and $\mathbf{B}$ matices. Several linear relationships were shown to exist including $[r_{turn}, \dot{u}]$, and $[r_{turn}, \dot{\psi}]$. The steady turn discussed here has been observed in scaled versions of the robotic samara. Therefore the open-loop control demonstrated and analyzed is considered to be appropriate for similar vehicles of reduced size with limited sensing and actuation capabilities.

VI. Acknowledgments

This work was funded by the A. James Clark School of Engineering. The authors would like to acknowledge support from the University of Maryland Autonomous Vehicle Laboratory and Morpheus Laboratory for their continued teamwork and motivation. The authors would also like to thank RoboSeed, LLC for building an aircraft which has enabled progress in the flight dynamics and control of this unique UAV.

References

[1] Defense Sciences Office Nano Air Vehicle. Technical Report W31P4Q-06-C-0324, DARPA, September 2009.

[2] D. Pines and F. Bohorquez. Challenges Facing Future Micro-Air-Vehicle Development. *Journal of Aircraft*, 43:290–305, 2006.

[3] F. Graham. *Monocopters*. Perigee Press, East Liverpool Ohio, 1999.

[4] S. Jameson, N Allen, and H. Youngren. SAMARAI Nano Air Vehicle - A Revolution in Flight. In *DARPA contract W31P4Q-06-C-0324*, 2007.

[5] E.R. Ulrich and D. Pines. Effects of Planform Geometry on Mechanical Samara Autorotation Efficiency and Rotational Dynamics. *Journal of the American Helicopter Society*, page in press, 2010.

[6] E.R. Ulrich and D. Pines. Planform Geometric Variation, and its Effect on the Autorotation Efficiency of Mechanical Samara. In *AHS64th Annual Forum*, 2008.

[7] E.R. Ulrich, D. Pines, and J. Park. Mechanical Samara Deployment and Passive Distribution by a Fixed Wing Unmanned Air Vehicle. In *The AHS International Specialists Meeting on Unmanned Rotorcraft*, 2009.

[8] E.R. Ulrich, D. Pines, and S. Gerardi. Autonomous Flight of a Samara MAV. In *AHS65th Annual Forum*, 2009.

[9] E.R. Ulrich, D. Pines, and J.S Humbert. Pitch and Heave Control of Robotic Samara Micro-Air-Vehicles. *Journal of Aircraft*, page in press, 2010.

[10] J. Gordon Leishman. *Principal of Helicopter Aerodynamics*. Cambridge University Press, 2006.

[11] V. Klein and E. Morelli. *Aircraft System Identification*. AIAA, 2006.